Analysis and Modeling of the Multi-wavelength Observations of the Luminous GRB 190114C

N. Fraija[1] , S. Dichiara[2,3], A. C. Caligula do E. S. Pedreira[1], A. Galvan-Gamez[1], R. L. Becerra[1] , R. Barniol Duran[4], and B. B. Zhang[5,6]

[1] Instituto de Astronomía, Universidad Nacional Autónoma de México, Apdo. Postal 70-264, Cd. Universitaria, Ciudad de México 04510, México
nifraija@astro.unam.mx
[2] Department of Astronomy, University of Maryland, College Park, MD 20742-4111, USA
[3] Astrophysics Science Division, NASA Goddard Space Flight Center, 8800 Greenbelt Road, Greenbelt, MD 20771, USA
[4] Department of Physics and Astronomy, California State University, Sacramento, 6000 J Street, Sacramento, CA 95819-6041, USA
[5] School of Astronomy and Space Science, Nanjing University, Nanjing 210093, People's Republic of China
[6] Key Laboratory of Modern Astronomy and Astrophysics (Nanjing University), Ministry of Education, People's Republic of China

Abstract

Very-high-energy (VHE; $\geqslant 10\,\mathrm{GeV}$) photons are expected from the nearest and brightest gamma-ray bursts (GRBs). VHE photons, at energies higher than 300 GeV, were recently reported by the MAGIC Collaboration for this burst. Immediately, GRB 190114C was followed up by a massive observational campaign covering a large fraction of the electromagnetic spectrum. In this Letter, we obtain the Large Area Telescope (LAT) light curve of GRB 190114C and show that it exhibits similar features to other bright LAT-detected bursts; the first high-energy photon ($\geqslant 100\,\mathrm{MeV}$) is delayed with the onset of the prompt phase and the flux light curve exhibits a long-lasting emission (much longer than the prompt phase) and a short-lasting bright peak (located at the beginning of long-lasting emission). Analyzing the multi-wavelength observations, we show that the short-lasting LAT and Gamma-Ray Burst Monitor bright peaks are consistent with the synchrotron self-Compton reverse-shock model, and that the long-lasting observations are consistent with the standard synchrotron forward-shock model that evolves from a stratified stellar-wind–like medium to a uniform interstellar-medium–like medium. Given the best-fit values, a bright optical flash produced by synchrotron reverse-shock emission is expected. From our analysis we infer that the high-energy photons are produced in the deceleration phase of the outflow, and some additional processes to synchrotron in the forward shocks should be considered to properly describe the LAT photons with energies beyond the synchrotron limit. Moreover, we claim that an outflow endowed with magnetic fields could describe the polarization and properties exhibited in the light curve of GRB 190114C.

Key words: acceleration of particles – gamma-ray burst: individual (GRB 190114C) – ISM: general – magnetic fields – radiation mechanisms: non-thermal

1. Introduction

Gamma-ray bursts (GRBs), the most luminous gamma-ray transient events in the universe, are non-repeating flashes that are usually associated with the core collapse of massive stars when the duration of the prompt emission is longer than $\gtrsim 2\,\mathrm{s}$, or to the merger of compact object binaries when the duration is less than $\lesssim 2\,\mathrm{s}$ (e.g., see Zhang & Mészáros 2004; Kumar & Zhang 2015, for reviews). Irrespective of the progenitor associated to the prompt emission, a long-lasting afterglow emission is generated via the deceleration of the outflow in the cirbumburst medium. The transition between the prompt and afterglow phase is recognized by early signatures observed in multi-wavelength light curves and broadband spectral energy distributions (SEDs). These signatures are associated with abrupt changes in the spectral features (Giblin et al. 1999), the sudden decrease in the density flux interpreted as high-latitude emission (Kumar & Panaitescu 2000; Fraija et al. 2019a), rapid variations in the evolution of the polarimetric observations (Granot 2003; Fraija et al. 2017a; Troja et al. 2017), and an outstanding multi-frequency peak generated by the reverse shock (Kobayashi & Zhang 2007; Fraija et al. 2016a; Fraija & Veres 2018; Becerra et al. 2019a).

The detection of very-high-energy (VHE; $\gtrsim 10\,\mathrm{GeV}$) photons and their arrival times provides a crucial piece of information to quantify the baryonic composition of the outflow, the particle acceleration efficiency, the emitting region, and the radiation processes, among others (e.g., see Zhang & Mészáros 2004; Kumar & Zhang 2015, for reviews). The Large Area Telescope (LAT) on board the *Fermi* satellite has detected more than 100 GRBs that exhibited photons greater than $\geqslant 100\,\mathrm{MeV}$, and only one dozen bursts with VHE ($\geqslant 10\,\mathrm{GeV}$) photons. The most powerful bursts have shown that the energetic photons arrive late with respect to the onset of the prompt emission, and the LAT light curves display two distinct components: one that lasts much longer than the prompt emission (called long-lasting emission), and another short-lasting bright peak located at the beginning of the long-lasting emission. Using multi-wavelength observations at lower energies for these powerful events, several authors modeled the long-lasting emission with the standard synchrotron forward-shock model (Kumar & Barniol Duran 2009, 2010; Zou et al. 2009; Ghisellini et al. 2010; Nava et al. 2014; Becerra et al. 2017), and the short-lasting bright peak with the synchrotron self-Compton reverse-shock model (Fraija 2015a; Fraija et al. 2016a, 2017a), indicating that the LAT fluxes were generated during the external shocks. However, this is not the case for VHE photons, which cannot be interpreted in the framework of the synchrotron forward-shock model. The maximum photon energy generated by this radiative process is $\sim 10\,\mathrm{GeV}\left(\frac{\Gamma}{100}\right)(1+z)^{-1}$, where Γ is the bulk Lorentz factor

and z the redshift (Abdo et al. 2009a; Piran & Nakar 2010; Barniol Duran & Kumar 2011). Given that the bulk Lorentz factor evolves during the afterglow as $\propto t^{-\frac{3}{8}}$ and $\propto t^{-\frac{1}{4}}$ for a uniform interstellar-medium (ISM)-like medium and a stratified stellar-wind–like medium, respectively, VHE photons from synchrotron radiation are not expected at the end of this phase. Therefore, we want to emphasize that the LAT photons below the maximum synchrotron energy can be explained well by synchrotron forward shock; beyond the synchrotron limit, some additional mechanisms must be invoked to explain the VHE LAT photons.

The BAT (Burst Area Telescope) instrument on board the *Swift* satellite triggered on GRB 190114C on 2019 January 14 at 20:57:06.012 UTC (trigger 883832; Gropp et al. 2019). GRB 190114C was also detected by the two instruments on board the *Fermi* satellite; Gamma-Ray Burst Monitor (GBM; Kocevski et al. 2019) and LAT (Kocevski et al. 2019). Immediately after the detection, counterparts were observed by the X-ray Telescope (XRT; Gropp et al. 2019; Osborne et al. 2019) and Ultraviolet/Optical Telescope (UVOT; Gropp et al. 2019; Siegel et al. 2019) on board the *Swift* satellite, the SPI-ACS instrument on board the *International Gamma-ray Astrophysics Laboratory* (*INTEGRAL*; Minaev & Poza-nenko 2019), the Mini-CALorimeter instrument on board the Astrorivelatore Gamma ad Immagini ultra LEggero (AGILE) satellite (Ursi et al. 2019), the Hard X-ray Modulation Telescope instrument on board the Insight satellite (Xiao et al. 2019), the Konus-Wind (Frederiks et al. 2019), the the Atacama Large Millimeter/submillimeter Array (ALMA), the Very Large Array (VLA; Laskar et al. 2019), and by a massive campaign of optical instruments and telescopes (Alexander et al. 2019; Bolmer & Shady 2019; D'Avanzo et al. 2019; Im et al. 2019a, 2019b; Izzo et al. 2019; Kim & Im 2019a, 2019b; Kumar et al. 2019; Lipunov et al. 2019; Mazaeva et al. 2019; Mirzoyan et al. 2019; Selsing et al. 2019; Tyurina et al. 2019). For the first time an excess of gamma-ray events with a significance of 20σ was detected during the first 20 minutes and photons with energies above 300 GeV were reported by the MAGIC Collaboration from GRB 190114C (Mirzoyan et al. 2019).

In this Letter, we analyze the LAT light curve obtained at the position for GRB 190114C and show that it exhibits similar features of other LAT-detected bursts. Analyzing the multi-wavelength observations, we show that the short-lasting LAT and GBM bright peaks are consistent with synchrotron self-Compton reverse-shock model and the long-lived LAT, GBM, X-ray, optical, and radio emissions with the synchrotron forward-shock model that evolves from a stratified stellar-wind–like medium to a uniform ISM-like medium. This Letter is arranged as follows. In Section 2 we present multi-wavelength observations and/or data reduction. In Section 3 we describe the multi-wavelength observations through the synchrotron forward-shock model and the SSC reverse-shock model in a stratified stellar-wind–like and a uniform ISM-like medium. In Section 4, the discussion and results of the analysis executed using the multi-wavelength data are presented. Finally, in Section 5 we give a brief summary. The convention $Q_x = Q/10^x$ in cgs units and the universal constants $c = \hbar = 1$ in natural units will be adopted throughout this Letter.

2. GRB 190114C: Multi-wavelength Observations and/or Data Reduction

2.1. Fermi-*LAT Observations and Data Reduction*

The *Fermi*-LAT instrument detected VHE emission from GRB 190114C. LAT data exhibited a representative increase in the event rate. The preliminary photon index above 100 MeV was $\Gamma_{\rm LAT} = \beta_{\rm LAT} + 1 = 1.98 \pm 0.06$, with an estimated energy flux of $(2.06 \pm 0.14) \times 10^{-6}\,{\rm erg\,cm^{-2}\,s^{-1}}$. Later, Wang et al. (2019) analyzed the LAT spectrum in two time intervals, $\sim$6–7 s and 11–14 s, reporting power-law (PL) indexes of $\Gamma_{\rm LAT} = \beta_{\rm LAT} + 1 = 2.06 \pm 0.30$ and 2.10 ± 0.31, respectively.

Fermi-LAT event data files are retrieved from the online data repository[7] starting few seconds before the GBM trigger time, 20:57:02.63 UT (Hamburg et al. 2019). These data are analyzed using Fermi Science tools[8] version v11r06p03 and reprocessed with Pass 8 extended, spacecraft data, and the instrument response functions "P8R3_TRANSIENT020_V2." Transient events are selected using *gtselect* (evtclass = 16) in the energy range between 100 MeV and 300 GeV, within 15° of the reported GRB position and with a maximum zenith angle of 100°. After taking into account of a model for the source and diffuse components (galactic and extragalactic) using *gtdiffrsp*, we generate the spectra and related response files using *gtbin* and *gtrspgen*, respectively. Data are binned in seven time bins: [1–5, 5–10, 10–15, 15–35, 35–65, 65–90, 90–150] s from the trigger. This binning pattern results from a trade-off aimed to preserve the time profile of the signal and the minimum statistical significance needed to analyze the spectrum. We derive the spectrum for each bin and fit it with a simple power law (SPL) using the software XSPECv12.10.1 (Arnaud 1996). The resulting fluxes are computed after the fit with 90% confidence errors in each time bin. The light curves with the flux above 100 MeV are shown in the upper panel of Figure 1.

Figure 1 shows the *Fermi*-LAT energy flux (blue) and photon flux (red) light curves obtained between 0.1 and 300 GeV (upper panel) and the energies of all the photons ($\geqslant$100 MeV) with probabilities >90% of being associated with this burst (lower panel). In the upper panel we can observe that the energy flux and the photon flux light curves exhibit a bright peak at $\sim$6–7 s followed by a monotonic decreasing emission extended for $\sim$70 s.

In order to model the *Fermi*-LAT data, the function (Vestrand et al. 2006)

$$F(t) = A\left(\frac{t - t_0}{t_0}\right)^{-\alpha_{\gamma,\rm pk}} e^{-\frac{\tau}{t - t_0}},\qquad(1)$$

and an SPL ($\propto t^{-\alpha_{\rm LAT}}$) are used to describe the short-lasting bright peak and the long-lasting emission, respectively. Here, t_0 is the starting time, A is the amplitude, τ is the timescale of the flux rise, and $\alpha_{\gamma,\rm pk}$ is the temporal decay index of the peak. The energy flux light curve, together with the best-fit curve, are shown in this upper panel. The best-fit values found are $t_0 = 2.61 \pm 0.15$ s, $\tau = 8.11 \pm 1.22$ s, $\alpha_{\gamma,\rm pk} = 2.65 \pm 0.19$ and $\alpha_{\rm LAT} = 1.10 \pm 0.15$ ($\chi^2 = 0.86$).

The lower panel in Figure 1 displays several features. (i) The first high-energy photon of 571.4 MeV that was observed at

---
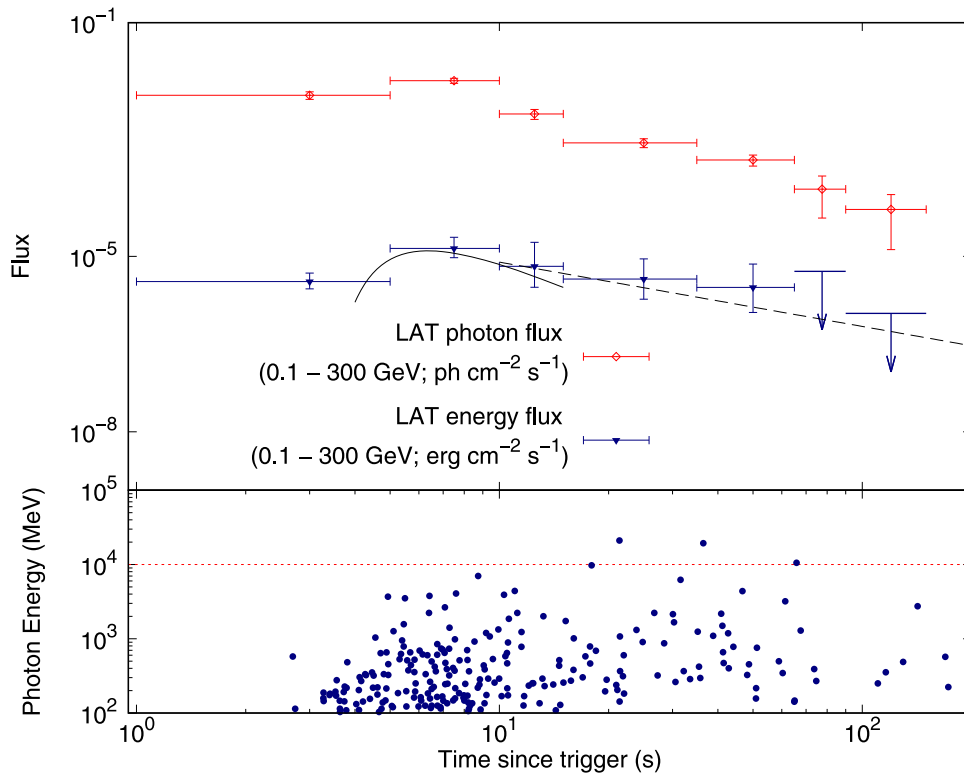
Figure 1. Upper panel: *Fermi*-LAT energy flux (blue) and photon flux (red) light curves obtained between 0.1 and 300 GeV. The solid black line represents the best-fit curve found using our model. Lower panel: all the photons with energies >100 MeV and probabilities >90% of being associated with GRB 190114C. *Fermi*-LAT data were reduced using the public database at the *Fermi* website.

2.7 s after the GBM trigger. (ii) This burst exhibited 238 photons with energies larger than 100 MeV, 41 with energies larger than 1 GeV, and five with energies larger than 10 GeV. (iii) The highest-energy photon exhibited in the LAT observations was 21.42 GeV detected at 21 s after the GBM trigger.[9]

2.2. GBM Observations

The *Fermi* GBM instrument triggered and localized GRB 190114C at 2019 January 14 20:57:02.63 UTC. During the first 15 s after the trigger, the GBM light curve showed a very bright, multi-peaked pulse followed by a weaker pulse occurring between 15 and 25 s. In addition, a fainter emission with a duration of 200 s after the trigger was detected. The GBM team reported a duration of the main emission of $T_{90} = 116$ s (50–300 keV). This burst presented an equivalent isotropic energy of 3×10^{53} erg in the energy range of 1 keV–10 MeV (Hamburg et al. 2019).

Recently, Ravasio et al. (2019) analyzed the GBM data, finding two different spectral components: a smoothly broken PL (SBPL) and a PL. Authors showed that the EPL component in the energy range of 10 keV–40 MeV reached the maximum flux (at the peak) of $(1.7 \pm 0.2) \times 10^{-5}$ erg cm^{-2} s in the time interval of $\sim$6–7 s. After the peak, this component decreased with a temporal index of 2.8 up to 15 s and finally, with 1. They reported a spectral PL index for the GBM spectrum of $\Gamma_{\rm GBM} = \beta_{\rm GBM} + 1 = 1.81 \pm 0.08$

Given the similarity between the LAT (see Figure 1) and GBM (see Figure 1 in Ravasio et al. 2019) light curves, we take the *Fermi* GBM data reported in Ravasio et al. (2019) and

model the EPL component. Again, the function described by Equation (1) and a SPL ($\propto t^{-\alpha_{\rm GBM}}$) are used to describe the short-lasting peak and the long-lasting emission, respectively. In this case, the best-fit values found are $t_0 = 3.09 \pm 0.23$ s, $\tau = 7.29 \pm 0.46$ s, $\alpha_{\gamma,\rm pk} = 2.96 \pm 0.19$ and $\alpha_{\rm GBM} = 1.05 \pm 0.13$ ($\chi^2 = 1.33$). The values obtained with our model are very similar to those ones reported by Ravasio et al. (2019).
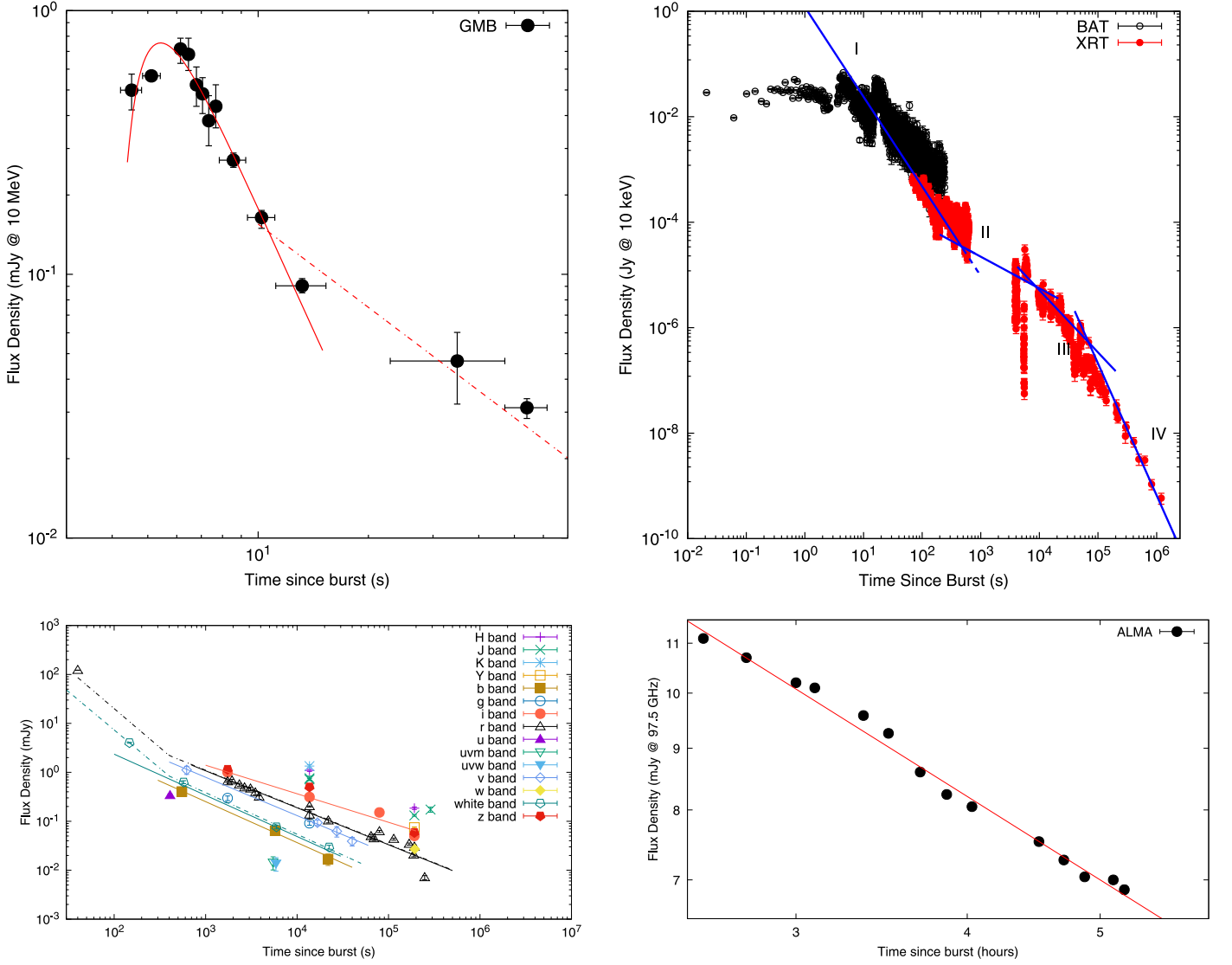
The upper left-hand panel in Figure 2 shows the GBM light curve of the EPL component at 10 MeV. The continuous and dashed red lines correspond to the best-fit curves. Data were taken from Ravasio et al. (2019).

2.3. X-Ray Observations and Data Reduction

The *Swift* BAT instrument triggered on GRB 190114C at 2019 January 14 20:57:06.012 UTC (Gropp et al. 2019). During the first 25 s, the BAT light curve exhibited a very bright multi-peaked structure. The main brightest emission consist of two complex pulses, ending at about 50 s after the trigger time. Afterward, the X-ray flux appeared to decay exponentially out to beyond 720 s after the trigger, when the burst went out of the BAT field of view. GRB 190114C returned to the BAT field of view at $\sim$3800 s after the trigger, although no significant flux was detected at that time (Krimm et al. 2019).

The *Swift* XRT instrument began observing GRB 190114C at 64 s after the trigger time. This instrument found a bright, uncatalogued X-ray source from 03:38:01.20 to 26:56:47.6 (J2000) with a 90% uncertainty radius of 1.4 arcsec (Gropp et al. 2019; Osborne et al. 2019).

The upper right-hand panel in Figure 2 shows the *Swift* X-ray light curve obtained with *Swift* BAT (black) and XRT

---

[9] It is worth noting that photons at energy higher than $\sim$300 GeV were reported by MAGIC Collaboration.

Figure 2. The upper left-hand panel shows the GBM light curve at 10 MeV. The solid red line corresponds to the best-fit curve using Equation (1), and the dashed red line corresponds to an SPL. Data were taken from Ravasio et al. (2019). The upper right-hand panel shows the X-ray light curve obtained with *Swift* BAT (black) and XRT (red) instruments at 10 keV. Blue lines correspond to the best-fit curves using SPL functions. The *Swift* data were obtained using the publicly available database on the official *Swift* website. The lower left-hand panel shows the optical light curves of GRB 190114C in different filters with the best-fit functions. The continuous line corresponds to the best-fit curve using an SPL function, and the dotted–dashed line using a broken PL (BPL) function. Optical data were collected from Izzo et al. (2019), Mirzoyan et al. (2019), Bolmer & Shady (2019), Im et al. (2019a), Alexander et al. (2019), D'Avanzo et al. (2019), Kim & Im (2019a), Kumar et al. (2019), Kim & Im (2019b), Im et al. (2019b), and Mazaeva et al. (2019). The lower right-hand panel shows the radio light curve obtained with ALMA at 97.5 GHz. The red line corresponds to the best-fit curve using an SPL function. Radio data were taken from Laskar et al. (2019).

(red) instruments at 10 keV. Blue lines correspond to the best-fit curves using SPL functions. *Swift* data were obtained using the public available database at the official *Swift* website. Four PL segments are identified in the X-ray light curve. (I) An initial PL segment with a temporal index of 1.59 ± 0.12. This value clearly is not related with the typical decay slope, which is explained in terms of the high-latitude emission of the prompt GRB (the emission has abruptly ceased; Kumar & Panaitescu 2000). (II) A PL segment with a temporal index of 0.57 ± 0.09. This value is consistent with shallow "plateau" decay segment (Zhang et al. 2006; Stratta et al. 2018). (III) A PL segment with a temporal index of 1.09 ± 0.11 (Zhang et al. 2006). This value is consistent with the normal decay segment. (IV) A late steeper decay with a temporal PL index of 2.54 ± 0.14. This value is consistent with the jet break

Table 1
Swift X-Ray Light Curve of GRB 190114C with the Best-fit Values of the Temporal PL Index with their Respective χ^2/NDF

X-Rays (PL Function)	Period	Index (α_X)	χ^2/ndf
I	$\leqslant 400$ s	1.59 ± 0.12	0.6
II	$400-10^4$ s	0.57 ± 0.09	0.81
III	10^4-10^5 s	1.09 ± 0.11	0.83
IV	$\geqslant 10^5$ s	2.54 ± 0.14	0.91

(Vaughan et al. 2006). The best-fit values of the X-ray data are reported in Table 1.

Table 2
Optical Light Curves of GRB 190114C in Different Filters with the Best-fit
Values of the Temporal PL Index with their Respective χ^2/NDF

Optical Band	Index α_O	Break Time t_{br}(s)	Index α_O	χ^2/ndf
b	⋯	⋯	0.8374 ± 0.0064	0.61
i	⋯	⋯	0.5835 ± 0.0089	1.32
r	⋯	⋯	0.7554 ± 0.0073	1.41
	1.593 ± 0.012	8.1	0.7554 ± 0.0034	1.22
v	⋯	⋯	0.7828 ± 0.0551	0.41
White	⋯	⋯	0.912 ± 0.0719	1.45
	1.567 ± 0.097	26.3	0.911 ± 0.081	1.72

2.4. Optical Observations and Data Reduction

The *Swift* UVOT began observing a candidate afterglow of GRB 190114C at 73 s after the trigger trigger (Gropp et al. 2019). The observations using the near-ultraviolet (NUV) filters of the first few orbits indicated that the afterglow faded rapidly (Siegel et al. 2019).

Using the MASTER-IAC telescope, Tyurina et al. (2019) pointed to GRB 190114C 25 s after notice time and 47 s after trigger time. On their first set they found one optical transient within the *Swift* error-box (R.A. = 54.5042, decl. = −26.9383) that was brighter than 16.54 mag. Furthermore, MASTER-SAAO with MASTER-IAC telescopes reported a polarization photometry in four position angles (Lipunov et al. 2019). de Ugarte Postigo et al. (2019) detected a source in the Pan-STARRS archival in the field of GRB 190114C, suggesting that this source as the possible host galaxy of GRB 190114C. This was confirmed by NOT (Selsing et al. 2019), which derived a redshift of $z = 0.42$. Additional photometry was reported in Izzo et al. (2019), Mirzoyan et al. (2019), Bolmer & Shady (2019), Im et al. (2019a, 2019b), Alexander et al. (2019), D'Avanzo et al. (2019), Kim & Im (2019a, 2019b), Kumar et al. (2019), and Mazaeva et al. (2019).

The lower left-hand panel of Figure 2 shows the optical light curves of GRB 190114C in different filters with the best-fit functions. The continuous line corresponds to the best-fit curve using an SPL function and the dotted–dashed line using a BPL function. SPL functions are used for the *i*, *r*, *v*, white, and *b* bands (solid lines) and BPL functions for the *r* and white bands (dotted–dashed lines). Optical data were collected from several instruments and taken from the GCN circulars showed above. The optical fluxes and their corresponding uncertainties used in this work were calculated using the standard conversion for AB magnitudes shown in Fukugita et al. (1996). The optical data were corrected by the galactic extinction using the relation derived in Becerra et al. (2019b). The values of $\beta_O = 0.83$ for optical filters and a reddening of $E_{B-V} = 0.01$ (Bolmer & Shady 2019) were used.

The best-fit values of the temporal PL indexes with their respective χ^2/ndf are reported in Table 2. This table shows that optical fluxes present two distinct decays separated by a break at ∼400 s. Before this break, the temporal PL indexes are stepper ($\alpha_O = 1.593 \pm 0.012$ for the *r*-band and 1.567 ± 0.097) and after they lie in the range of $0.6 \lesssim \alpha_O \lesssim 0.9$. Due to the large amount of optical data collected in the *r*-band, the multi-wavelength analysis is done considering the optical *r*-band data points. The *r*-band optical observation collected the ninth day after the burst trigger was removed due to the contamination by the host galaxy and supernova associated with this burst (Burenin et al. 2019; Melandri et al. 2019).

2.5. Radio Observations

ALMA (at 97.5 GHz) and the Karl G. Jansky VLA (at 5–38 GHz) began observing the afterglow of GRB 190114C at 2.2 and 4.7 hr after the burst trigger, respectively (Laskar et al. 2019). The ALMA and VLA observations were extended up to 5.2 and 6.3 hr after the burst trigger, respectively. Authors described the SED of the radio data at 0.2 days; VLA at radio cm-band and ALMA at mm-band. Using a BPL model they found a spectral index of $\beta_R = 0.3 \pm 0.2$ below the break of 24 ± 4 GHz. In addition, (Laskar et al. 2019) found that the GROND *K*-band and ALMA observations were consistent with a SPL at 0.16 days. The lower right-hand panel in Figure 2 shows the radio light curves of the ALMA observations with the best-fit curve using a SPL function. The best-fit value of the temporal index of 0.71 ± 0.01 is reported in Table 3. Radio data were taken from Laskar et al. (2019).

2.6. VHE Observations

MAGIC telescopes detected VHE gamma-ray emission from GRB 190114C. Their data showed a clear excess of gamma-ray events with the significance 20σ in the first 20 minutes (starting at $T + 50$ s) for photon energies around 300 GeV. Other TeV gamma-ray observatories such as the High Altitude Water Cherenkov (HAWC) and H.E.S.S. reported neither VHE detection nor upper limits in the directions of GRB 190114C.

3. Description of the Multi-wavelength Observations

3.1. Multi-wavelength Analysis of Observations

Figure 3 shows the LAT, GBM, X-ray, optical, and radio light curves (upper panel) and the broadband SED of the X-ray and optical (UVOT) observations during the period of 5539–57216 s (lower panel) of GRB 190114C with the best-fit curves. The shaded period in the upper panel corresponds to the spectrum on the lower panel. The best-fit values of the temporal PL indexes obtained through the chi-square χ^2 minimization function are reported in Table 3. In order to obtain the best-fit values of the spectral PL indexes, we analyze the broadband SED of GRB 190114C, taking into account the available X-ray and optical data, and the values reported for the LAT, GBM, and radio bands.

During the first 70 s, the observations are almost covered by the LAT and GBM instruments with only one optical (*r*-band) data point. The LAT collaboration reported a spectral PL index above 100 MeV of $\beta_{LAT} = 1.98 \pm 0.06$ (Kocevski et al. 2019). Analyzing the LAT spectrum, Wang et al. (2019) reported PL indexes of $\beta_{LAT} = 1.06 \pm 0.30$ and 1.10 ± 0.31 for two time intervals ∼6–7 s and 11–14 s, respectively. Analyzing the PL component of the GBM data, Ravasio et al. (2019) reported a spectral index of $\beta_{GBM} = 0.81 \pm 0.08$. From 70 to 400 s, X-rays dominate the observations with one optical data point in the white band.

During the time interval from 5539 to 57216 s, the optical (UVOT) and X-ray (XRT) available data are quasi-simultaneous, as shown in the lower panel in Figure 3. From X-ray to optical data, the SED is modeled with a SPL with PL index $\beta_X = 0.83 \pm 0.04$. The blue dashed line is the best-fit curve

Table 3
The Best-fit Values of the Spectral and Temporal Indexes Using the LAT, X-Ray and Optical Observational Data

	Observation ($\leqslant 400$ s)	Theory (Stratified Medium)	Observation ($400-10^4$ s)	(10^4-10^5 s)	Theory (Uniform Medium)		Observation ($\geqslant 10^5$ s)	Theory (Uniform Medium)
LAT flux								
α_{LAT}	1.10 ± 0.15	1.15 ± 0.22	...		...		...	...
β_{LAT}	1.10 ± 0.31[a]	1.10 ± 0.15	...		...		–	–
GBM flux								
α_{GBM}	1.05 ± 0.13	1.15 ± 0.22	...		...		...	...
β_{GBM}	0.81 ± 0.08[b]	1.10 ± 0.15	...		...		...	...
X-ray flux	I		II	III	II	III	IV	
α_X	1.59 ± 0.12	1.40 ± 0.22	0.57 ± 0.09	1.09 ± 0.11	$(0.1-0.6)$	1.15 ± 0.22	2.54 ± 0.14	2.2 ± 0.3
β_X	...	...		0.83 ± 0.04		0.60 ± 0.15	...	...
Optical flux								
α_O	1.593 ± 0.012	1.40 ± 0.22		0.755 ± 0.003		0.90 ± 0.22	...	...
β_O	...	...		0.83 ± 0.04		0.60 ± 0.15	...	...
Radio flux								
α_R	...	...		0.71 ± 0.01		0.90 ± 0.22	...	...
β_R	...	...		$-(0.3 \pm 0.2)$[c]		-0.33[d]	...	...

Notes. In addition, the theoretical predictions of the spectral and temporal indexes are calculated for $p = 2.2 \pm 0.3$. Values in round parentheses are the chi-square minimization (χ^2/N.D.F.).
[a] This value was reported in Wang et al. (2019).
[b] This value was reported in Ravasio et al. (2019).
[c] This value was reported in Laskar et al. (2019) below 24 GHz. Above this value, the radio mm-band and optical data can be described with an SPL.
[d] The value between radio mm-band and optical data is 0.60 ± 0.15.

obtained from XSPEC. During this period, Laskar et al. (2019) described the SED of the radio data at 0.2 days: VLA at radio cm-band and ALMA at mm-band. Using a BPL model they found a value of spectral index $\beta_R = 0.3 \pm 0.2$ below a break of 24 ± 4 GHz. In addition, the authors found that the GROND K-band and ALMA observations were consistent with an SPL at 0.16 days. For the period of time longer than 57216 s, it is not possible to analyze the multi-wavelength observations because there is no quasi-simultaneous available data. The best-fit values of the temporal and spectral PL indexes of the LAT, GBM, X-ray, optical, and radio fluxes are reported in Table 3.

3.2. Synchrotron Forward-shock Model and Analysis of the Long-lasting Multi-wavelength Observations

3.2.1. Light Curves in a Stratified Stellar-wind–like Medium

Taking into consideration a Wolf–Rayet (WR) star as progenitor with typical values of a mass-loss rate of $\dot{M} \simeq 10^{-6} M_\odot \, \mathrm{yr}^{-1}$ and a constant wind velocity of $v_W \simeq 10^8$ cm s^{-1}, the density of the stratified stellar-wind–like medium is given by $\rho(r) = A \, r^{-2}$, where $A = \frac{\dot{M}}{4\pi v_W} = A_\star \, (5 \times 10^{11})$g cm^{-1} with $A_\star$ a parameter of stellar wind density (Dai & Lu 1998; Chevalier & Li 2000; Panaitescu & Kumar 2000; Vink et al. 2000; Chevalier et al. 2004; Vink & de Koter 2005). Using the typical timescales together with the maximum power emitted by relativistic electrons, the characteristic (for $p \geqslant 2$) and cooling energy breaks and the maximum flux evolve as $\epsilon_{m,f}^{syn} \propto t^{-\frac{3}{2}}$, $\epsilon_{c,f}^{syn} \propto t^{\frac{1}{2}}$ and $F_{max,f}^{syn} \propto t^{-\frac{1}{2}}$, respectively. The subscript f refers throughout this manuscript to the forward shock. The synchrotron

breaks and the maximum flux are functions of $\varepsilon_{e,f}$, $\varepsilon_{B,f}$, E, and A. The terms $\varepsilon_{e,f}$ and $\varepsilon_{B,f}$ refer to the microphysical parameters given to accelerate electrons and to amplify the magnetic field, respectively, E is the equivalent kinetic energy given by the isotropic energy $E_{\gamma,\mathrm{iso}}$ and the efficiency η to convert the kinetic to gamma-ray energy, and ξ is a constant parameter which lies in the range of $0.4 < \xi < 0.78$ (Panaitescu & Mészáros 1998; Chevalier & Li 2000). Given the synchrotron spectra for the fast- and slow-cooling regimes, together with the synchrotron spectral breaks and the maximum flux, the synchrotron light curves in the fast (slow)- cooling regime are

$$F_{\nu,f}^{syn} \propto \begin{cases} t^{-\frac{2}{3}}(t^0)\epsilon_\gamma^{\frac{1}{3}}, & \epsilon_\gamma < \epsilon_{c,f}^{syn}(\epsilon_{m,f}^{syn}), \\ t^{-\frac{1}{4}}\epsilon_\gamma^{-\frac{1}{2}}(t^{-\frac{3p-1}{4}}\epsilon_\gamma^{-\frac{p-1}{2}}), & \epsilon_{c,f}^{syn}(\epsilon_{m,f}^{syn}) < \epsilon_\gamma < \epsilon_{m,f}^{syn}(\epsilon_{c,f}^{syn}) \\ t^{-\frac{3p-2}{4}}(t^{-\frac{3p-2}{4}})\epsilon_\gamma^{-\frac{p}{2}}, & \epsilon_{m,f}^{syn}(\epsilon_{c,f}^{syn}) < \epsilon_\gamma < \epsilon_{max,f}^{syn}, \end{cases}$$

(2)

where ϵ_γ is the energy at which the flux is detected. Given the evolution of the bulk Lorentz factor in the stellar-wind–like medium $\Gamma \propto t^{-\frac{1}{4}}$, the maximum synchrotron energy in this case evolves as $\epsilon_{max,f}^{syn} \propto t^{-\frac{1}{4}}$.

3.2.2. Light Curves in a Uniform ISM–like Medium

The dynamics of the forward shocks for a relativistic outflow interacting with a homogeneous medium (n) is usually analyzed through the deceleration timescale and the equivalent kinetic energy evolved in the shock (e.g., see Sari & Piran 1995;
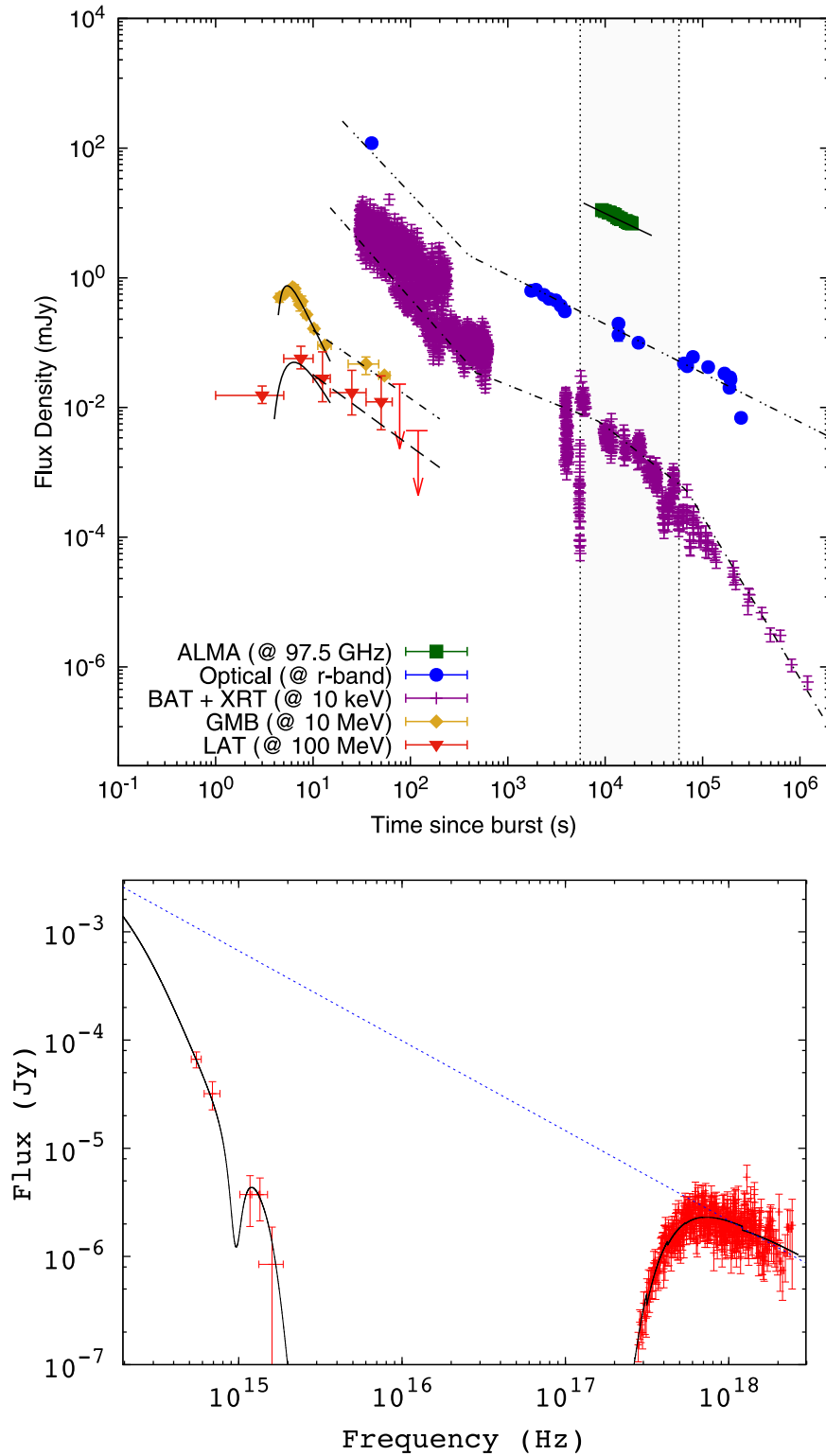
Figure 3. Top panel: light curves and fits of the multi-wavelength observation of GRB 190114C with the synchrotron forward-shock and SSC reverse-shock models. Bottom panel: the broadband SED of the X-ray and optical (UVOT) observations during the period of 5539–57216 s. The solid black line is the best-fit curve from XSPEC. The shaded period in the upper panel corresponds to the spectrum on the lower panel.

Sari et al. 1998; Sari & Piran 1999; Kumar & Piran 2000). Taking into account the typical timescales together with the maximum power emitted by the electron population, the synchrotron spectral breaks and the maximum flux evolve as $\epsilon_{m,f}^{syn} \propto t^{-\frac{3}{2}}$, $\epsilon_{c,f}^{syn} \propto t^{-\frac{1}{2}}$ and $F_{max,f}^{syn} \propto t^0$, respectively (Sari et al. 1998). Given the synchrotron spectra for the fast- and slow-

cooling regimes, together with the synchrotron spectral breaks and the maximum flux, the synchrotron light curves in the fast

(slow)-cooling regime are

$$
F_{\nu,\mathrm{f}}^{\mathrm{syn}} \propto
\begin{cases}
t^{\frac{1}{6}}\,(t^{\frac{1}{2}})\,\epsilon_{\gamma}^{\frac{1}{3}}, & \epsilon_{\gamma} < \epsilon_{\mathrm{c,f}}^{\mathrm{syn}}(\epsilon_{\mathrm{m,f}}^{\mathrm{syn}}), \\[2mm]
t^{-\frac{1}{4}}\epsilon_{\gamma}^{-\frac{1}{2}}(t^{-\frac{3p-3}{4}}\epsilon_{\gamma}^{-\frac{p-1}{2}})\ \epsilon_{\mathrm{c,f}}^{\mathrm{syn}}(\epsilon_{\mathrm{m,f}}^{\mathrm{syn}}) < \epsilon_{\gamma} < \epsilon_{\mathrm{m,f}}^{\mathrm{syn}}(\epsilon_{\mathrm{c,f}}^{\mathrm{syn}}) \\[2mm]
t^{-\frac{3p-2}{4}}(t^{-\frac{3p-2}{4}})\epsilon_{\gamma}^{-\frac{p}{2}}, & \epsilon_{\mathrm{m,f}}^{\mathrm{syn}}(\epsilon_{\mathrm{c,f}}^{\mathrm{syn}}) < \epsilon_{\gamma} < \epsilon_{\mathrm{max,f}}^{\mathrm{syn}},
\end{cases}
$$

$$(3)$$

where ϵ_{γ} is the energy at which the flux is detected. Given the evolution of the bulk Lorentz factor $\Gamma \propto t^{-\frac{3}{8}}$ in the forward shock, the maximum synchrotron energy evolves as $\epsilon_{\mathrm{max,f}}^{\mathrm{syn}} \propto t^{-\frac{3}{8}}$.

3.2.3. Analysis of Long-lasting Multi-wavelength Observations

Given the spectral and temporal indexes of the LAT, GBM, X-ray, optical, and radio bands, it can be observed from Table 3 that the evolution of synchrotron emission can be separated into four distinct periods.

During the first period ($t \lesssim 400\,\mathrm{s}$), the temporal decays of the optical and X-ray observations are equal and are steeper ($\Delta\alpha \sim 0.4$) than those of the LAT and GBM light curves. During this period, the spectral indexes of the LAT and GBM observations are each consistent within the uncertainties. It is worth noting that the temporal PL index of the X-ray light curve cannot be associated with the end of prompt emission that is larger than 2.5. We conclude that both the LAT and GBM observations evolve in the third PL segment, and the optical and X-ray fluxes evolve in the second PL segment of the slow-cooling regime in the stratified stellar-wind–like medium for $p = 2.2 \pm 0.3$.

During the second and third periods ($400 \lesssim t \lesssim 10^5$), the X-ray flux presents a chromatic break at $\sim 10^4\,\mathrm{s}$. During this transition, the temporal PL index varied from 0.57 ± 0.09 to 1.09 ± 0.11, while the spectral index remained unchanged. The temporal PL index after the break is consistent with the afterglow model evolving in a uniform IMS-like medium, while the temporal index before the break is associated with the "plateau" phase. It is worth mentioning that during this shallow-to-normal transition found in a large fraction of GRBs, the spectral index does not vary. During this period, the spectral analysis presented in this work reveals that the optical and X-ray observations are consistent with an SPL. Moreover, the temporal PL indexes of radio (ALMA) and optical observations are consistent each other, and the spectral analysis reported by Laskar et al. (2019) indicated that these observations are consistent with an SPL. Similarly, their analysis reported that the radio observations between VLA and ALMA are consistent with a BPL that has a break at 24 GHz. Therefore, we conclude that X-ray, optical, and radio (ALMA) fluxes evolve in the second PL segment between the cutoff and characteristic energy breaks, and the radio (VLA) evolves in first PL segment of the slow-cooling regime in the uniform ISM-like medium for $p = 2.2 \pm 0.3$.

During the four periods ($t \gtrsim 10^5$), the temporal index in the X-ray flux is consistent with the jet break.

The temporal and spectral theoretical indices obtained by the evolution of the standard synchrotron model in the stratified stellar-wind–like medium and in the uniform ISM-like medium are reported in Table 3. Theoretical and observational spectral and temporal indices are in agreement. The best explanation for this behavior is that the synchrotron radiation undergoes a phase transition from a stratified stellar-wind–like to a uniform ISM-like medium around $\sim 400\,\mathrm{s}$.

3.3. The SSC Reverse-shock Model and Analysis of the Short-lasting Bright LAT Peak

3.3.1. SSC Model in the Stratified Stellar-wind–like Medium

The quantities of synchrotron reverse-shock model such as the spectral breaks, fluxes, and light curves that describe the optical flashes are introduced in Chevalier & Li (2000). In the thick-shell case ($\Gamma < \Gamma_c$) where the deceleration time is assumed to be smaller than the duration of the prompt phase; the outflow is decelerated by the reverse shock are derived in Zhang & Kobayashi (2005). The term Γ_c is the critical Lorentz factor. The relationship among the characteristic energy breaks and maximum fluxes in the forward and reverse shocks were derived in Zhang & Kobayashi (2005).

The quantities of the SSC reverse-shock model as the spectral breaks, the fluxes, and the light curves have been widely explored (e.g., see, Wang et al. 2001a, 2001b; Veres & Mészáros 2012; Fraija et al. 2016a). In the thick-shell case, the SSC light curve at the shock crossing time (t_d) was presented in Fraija et al. (2016a). At $t < t_\mathrm{d}$, the SSC emission increases as $\propto t^{1/2}$ reaches at the shock crossing time the maximum value of $F_{\nu,\mathrm{r}} \sim F_{\nu,\mathrm{max,r}}\left(\frac{\epsilon_{\mathrm{LAT}}}{\epsilon_{\mathrm{c,r}}}\right)^{-\frac{1}{2}}$, where the energy range observed by the LAT instrument (ϵ_{LAT}) is constrained by the characteristic break ($\epsilon_{\mathrm{LAT}} < \epsilon_{\mathrm{m,r}}^{\mathrm{ssc}}$). After $t > t_\mathrm{d}$, the LAT flux initially evolves as $\propto t^{-\frac{p+1}{2}}$, later as $\propto t^{-\frac{5}{2}}$, and finally as $\propto t^{-\frac{p+4}{2}}$ induced by the angular time delay effect (Kumar & Panaitescu 2000; Kobayashi & Zhang 2003). The shock-crossing time can be estimated as $t_d \sim (\Gamma/\Gamma_c)^{-4}T_{90}$ (Kobayashi & Zhang 2007).

3.3.2. Analysis of the LAT/GBM-peak Observations

In order to model the *Fermi*-LAT/GBM data, the function given by Equation (1) was used (Fraija et al. 2017b). The best-fit values of $t_0 = 2.61 \pm 0.51\,\mathrm{s}$ and $3.09 \pm 0.23\,\mathrm{s}$ indicate the onset of the reverse shock as suggested by Vestrand et al. (2006). The values of the temporal decay indices of $\alpha_{\gamma,\mathrm{pk}} = 2.65 \pm 0.19$ and 2.96 ± 0.19 are consistent with the decay slope of the synchrotron/SSC reverse-shock emission from high latitudes (due to the curvature effect; Zhang et al. 2003; Fraija et al. 2017a, 2019a). The values of the bulk Lorentz factor and the parameter of the stellar wind density can be constrained through the deceleration time $t_{\mathrm{dec}} \propto (1+z)\xi^{-2}\,E\,A^{-1}\,\Gamma^{-4}$ with the LAT/GBM-peak flux at ~ 6–$7\,\mathrm{s}$ and the critical Lorentz factor in the thick-shell regime $\Gamma > \Gamma_c$ (Zhang et al. 2003). In the thick-shell regime, the shock-crossing time is $t_d \sim (\Gamma/\Gamma_c)^{-4}T_{90} \simeq 6$–$7\,\mathrm{s}$ (Kobayashi & Zhang 2007), which is much shorter than the duration of the main burst. The peak of the LAT and GBM fluxes will be modeled with $F_{\nu,\mathrm{r}} \sim F_{\nu,\mathrm{max,r}}\left(\frac{\epsilon_{\gamma}}{\epsilon_{\mathrm{c,r}}^{\mathrm{ssc}}}\right)^{-\frac{1}{2}}$ (Zhang et al. 2003; Fraija et al. 2016b) and the value of the spectral index of electrons $p = 2.2 \pm 0.3$ found with multi-wavelength observations and synchrotron forward-shock model will be used. We want to emphasize that the synchrotron emission from the reverse shock is usually invoked to describe early optical afterglows (Kobayashi 2000; Kobayashi & Zhang 2003; Fraija et al. 2016a), so the SSC emission used in this work is required to describe the LAT/GBM-peak observations.

Table 4
Median Values of Parameters Found with Symmetrical Quantiles (15%, 50%, 85%); Our Model was used to Constrain the Values of Parameters

Parameters	Median				
	LAT (100 MeV)	GBM (10 MeV)	X-ray (10 keV)	Optical (1 eV)	Radio (97.5 GHz)
$A_\star(10^{-2})$	$5.999^{+0.297}_{-0.295}$	$6.149^{+0.298}_{-0.296}$	$6.101^{+0.099}_{-0.101}$	$5.950^{+0.098}_{-0.099}$	$6.000^{+0.100}_{-0.100}$
$n(\text{cm}^{-3})$	...	...	$1.060^{+0.099}_{-0.101}$	$1.100^{+0.098}_{-0.096}$	$1.084^{+0.099}_{-0.097}$
$\epsilon_{\text{B,f}}(10^{-5.3})$	$1.001^{+0.302}_{-0.298}$	$1.200^{+0.301}_{-0.296}$	$1.148^{+0.304}_{-0.293}$	$0.951^{+0.298}_{-0.301}$	$0.993^{+0.228}_{-0.190}$
$\epsilon_{\text{e,f}}(10^{-2})$	$1.000^{+0.304}_{-0.303}$	$1.150^{+0.294}_{-0.302}$	$1.140^{+0.604}_{-0.585}$	$1.139^{+0.298}_{-0.297}$	$1.095^{+0.156}_{-0.137}$
$\epsilon_{\text{B,r}}(10^{-1})$	$1.000^{+0.304}_{-0.303}$	$0.999^{+0.298}_{-0.297}$	...	...	...
$\epsilon_{\text{e,r}}(10^{-1})$	$0.999^{+0.100}_{-0.099}$	$1.150^{+0.104}_{-0.100}$	...	...	...
p	$2.300^{+0.100}_{-0.099}$	$2.202^{+0.098}_{-0.098}$	$2.250^{+0.098}_{-0.101}$	$2.280^{+0.099}_{-0.101}$	$2.296^{+0.010}_{-0.010}$

3.4. Transition from a Stratified Stellar-wind–like to Uniform ISM-like Medium

As indicated in Section 3.2.1, the progenitor of GRB 190114C can be associated with the core collapse of a WR star, indicating that the circumburst medium close to the progenitor is principally composed by the stratified stellar wind of the WR. At a distance away from the parent a uniform medium is expected. Therefore, a transition phase between the stratified to uniform medium is expected at a distance larger than $\gtrsim 10^{-2}$ pc (Castor et al. 1975; Weaver et al. 1977; Fryer et al. 2006). Weaver et al. studied this phase, considering a four-region structure that includes (i) the unshocked stratified stellar-wind–like medium with density $\rho(r)$, (ii) a quasi-isobaric zone consisting of the stellar wind mixed with a small fraction of interstellar gas, (iii) a dense-thin shell formed by most of ISM, and (iv) the unshocked ambient ISM (see Figure 1 in Pe'er & Wijers 2006).

Taking into consideration an adiabatic expansion, two strong shocks are formed; these are the outer and inner shocks. The outer termination (forward) shock radius can be estimated as

$$R_{\text{FS},W} = 1.2 \times 10^{19} \text{ cm } \dot{M}_{-6}^{\frac{1}{5}} v_{W,8}^{\frac{2}{5}} n^{-\frac{1}{5}} t_{\star,5}^{-\frac{3}{5}}, \quad (4)$$

where $t_\star$ is the lifetime of the WR.

The inner (reverse) shock radius for which the transition from stratified to uniform medium occurs (R_{tr}; Pe'er & Wijers 2006) is obtained by equaling the pressures in regions (ii) and (iii) (e.g., see, Pe'er & Wijers 2006; Garcia-Segura & Franco 1996)

$$P_{\text{(ii)}} = P_{\text{(iii)}} = 1.4 \times 10^{-11} \text{ dynes cm}^{-2} \dot{M}_{-6}^{\frac{2}{5}} v_{W,8}^{\frac{4}{5}} n^{-\frac{3}{5}} t_{\star,5}^{\frac{4}{5}}. \quad (5)$$

The distance from the progenitor to the wind-to-homogeneous transition is given by

$$R_{\text{tr}} \equiv R_{\text{RS},W} = 5.1 \times 10^{18} \text{ cm } \dot{M}_{-6}^{\frac{3}{10}} v_{W,8}^{\frac{1}{10}} n^{-\frac{3}{10}} t_{\star,5}^{\frac{2}{5}}. \quad (6)$$

The density of the stellar wind medium at $r = R_{\text{tr}}$ can be written as

$$\rho(R_{\text{tr}}) = 1.8 \times 10^{-27} \text{ g cm}^{-3} R_{\text{tr}}^{-2} \dot{M}_{-6} v_{W,8}^{-1}, \quad (7)$$

which corresponds to a particle number density of $\sim 10^{-3}$ cm^{-3}.

4. Results and Discussion

We show that temporal and spectral analysis of the long-lived multi-wavelength observations of GRB 190114C is consistent with the closure relations of the synchrotron

forward-shock model and the short-lasting LAT and GBM peaks with SSC reverse-shock model. The LAT and GBM observations favor the emission originated from the forward and reverse shocks in a stratified stellar-wind–like medium, and the X-ray and optical observations are consistent with the emission from forward shocks in both a stratified stellar-wind–like and a uniform ISM-like medium. The radio observations are consistent with the synchrotron emission radiated in a uniform ISM-like medium. The transition from the stratified to uniform medium is found to be around ~400 s after the GBM trigger. Now, we obtain the electron spectral index, the microphysical parameters, and the circumburst densities for which our model is satisfied. The photon energies of each PL segment at $\epsilon_\gamma = 97.5$ GHz, 1 eV, 10 keV, 10 MeV, and 100 MeV are considered to describe the radio, optical, X-ray, GBM, and LAT fluxes, respectively. We use the synchrotron light curves in the slow-cooling regime evolving in a stratified stellar-wind–like medium (Equation (2)) before $\lesssim 400$ s and in a uniform ISM-like medium (Equation (3)) after $\gtrsim 400$ s. The values reported of the observed quantities such as the redshift $z = 0.42$, the equivalent isotropic energy 3×10^{53} erg, and the duration of the prompt emission $T_{90} = 116$ s are required. In order to compute the luminosity distance, the values of cosmological parameters derived in Planck Collaboration et al. (2018) are used (Hubble constant $H_0 = (67.4 \pm 0.5)$ km s^{-1} Mpc^{-1} and the matter density parameter $\Omega_{\text{m}} = 0.315 \pm 0.007$). The equivalent kinetic energy is obtained using the isotropic energy and the efficiency to convert the kinetic to photons of $\eta = 0.15$ (Beniamini et al. 2015). The value of the parameter $\xi = 0.6$ was chosen when taking into account the range of values reported in the literature (Panaitescu & Mészáros 1998; Chevalier & Li 2000).

To find the best-fit values of the parameters that reproduce the multi-wavelength observations of GRB 190114C, we use the Bayesian statistical technique based on the Markov-chain Monte Carlo (MCMC) method (see Fraija et al. 2019b, 2019c, 2019d). The MCMC code computes the synchrotron forward-shock and the SSC reverse-shock models using, in general, a set of seven parameters, $\{A_\star, n, \epsilon_{\text{B,f}}, \epsilon_{\text{e,f}}, \epsilon_{\text{B,r}}, \epsilon_{\text{e,r}} \text{ and } p\}$. In particular, we use in each electromagnetic band only five parameters. For instance, the parameter $\{n\}$ is not used for the LAT and GBM observations, the parameters $\{\epsilon_{\text{B,r}} \text{ and } \epsilon_{\text{e,r}}\}$ are not used for radio, optical, and X-ray observations and the microphysical parameters $\{\epsilon_{\text{e,f}} \text{ and } \epsilon_{\text{B,f}}\}$ are used to fit the radio observations. A total of 16,000 samples with 4000 tuning steps were run. The best-fit value of each parameter for LAT, GBM, X-ray, optical, and radio observations is reported in Table 4. The obtained values are typical for those reported by other luminous GRBs
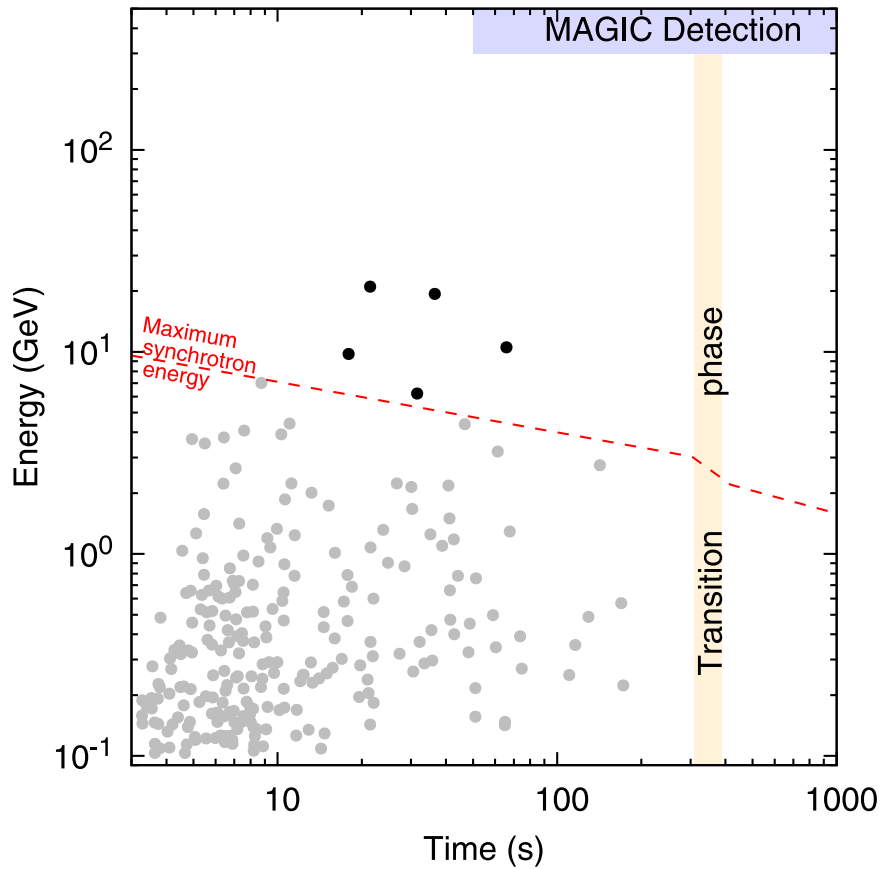
Figure 4. All the photons with energies >100 MeV and probabilities >90% of being associated with GRB 190114C. The red dashed line is the maximum photon energies released by synchrotron forward-shock model in a stratified stellar-wind–like medium and a uniform ISM-like medium. The yellow region represents the transition phase from a stratified to uniform medium and, the purple region the interval and the energy range of VHE photons reported by the MAGIC Collaboration. Photons with energy above the maximum synchrotron energy are in black, and those below are in gray.

(Ackermann et al. 2010, 2013, 2014; Fraija 2015a; Fraija et al. 2016a, 2016b, 2017a). Given the values of the observed quantities and the best-fit values reported in Table 4, the results are discussed as follows.

Taking into account the evolution of the maximum photon energy radiated by synchrotron emission from forward shock in both a stratified stellar-wind–like and a uniform ISM-like medium, and the best-fit values of both densities, we plot in Figure 4 all photons with energies larger than >100 MeV detected by *Fermi*-LAT and associated to GRB 190114C. In addition, this figure shows in a yellow region the transition from the stratified to uniform medium, and the interval and energy range of VHE photons (purple region) reported by the MAGIC Collaboration (Mirzoyan et al. 2019). Photons with energies above the maximum photon energy radiated by synchrotron emission (synchrotron limit) are in black, and those below are in gray. This figure shows that the standard synchrotron forward-shock model can hardy explain all photons, therefore this model has to be varied or some additional processes to synchrotron in the forward shocks, such as SSC emission, photo-hadronic interactions (Fraija 2014, 2015b) and proton synchrotron radiation, have to be evoked to interpret these VHE photons. We want to emphasize that the LAT photons below the maximum synchrotron energy (the red dashed line) can be interpreted in the synchrotron forward-shock framework and beyond the synchrotron limit some additional mechanisms must be present to explain the VHE LAT photons. It is worth noting that a

combination of synchrotron and SSC emission originating in the forward shock works well to explain the LAT photons (e.g., see Beniamini et al. 2015).

The best-fit values of the microphysical parameters found in forward- and reverse-shock regions are different. The microphysical parameter associated to the magnetic field in the reverse shock lies in the range of the expected values for the reverse shock to be formed and leads to an estimate of the magnetization parameter that is defined as the ratio of Poynting flux to matter energy flux $\sigma = \frac{L_{\rm pf}}{L_{\rm kn}} \simeq \frac{B_r^2}{4\pi\rho(r)\Gamma^2} \simeq 8\epsilon_{\rm B,r} \simeq 0.8$ (Drenkhahn 2002; Zhang & Kobayashi 2005). This value indicates that the outflow is magnetized. In a different situation (e.g., $\sigma \gg 1$), particle acceleration would be inefficient, and the LAT and GBM emissions from the reverse shock would have been suppressed (Fan et al. 2004). Considering the microphysical parameter associated with the magnetic field in the reverse-shock region, we found that the strength of magnetic field in this region is stronger that the magnetic field in the forward-shock region ($\simeq 20$ times). This suggests that the jet composition of GRB 190114C could be Poynting dominated. Zhang & Kobayashi (2005) described the emission generated in the reverse shock from an outflow with an arbitrary value of the magnetization parameter. They found that the Poynting energy is transferred to the medium only until the reverse shock has disappeared. Given the timescale of the reverse shock associated to the short-lasting LAT and GBM peaks (<100 s), the shallow decay segment observed in the X-ray light curve of

GRB 190114C might be interpreted as the late transferring of the Poynting energy to the uniform medium. This result agrees with the linear polarization reported in radio (Laskar et al. 2019) during the "plateau" phase. These results agree with some authors who claim that Poynting flux-dominated models with a moderate degree of magnetization can explain the LAT observations in several powerful GRBs (Zhang & Yan 2011; Uhm & Zhang 2014), and in particular the properties exhibited in the light curve of GRB 190114C.

Using the synchrotron reverse-shock model (Kobayashi 2000; Kobayashi & Zhang 2003) and the best-fit values found, the self-absorption, characteristic, and cutoff energy breaks of 4.5×10^{-8} eV, 0.5 eV, and 8.1×10^{-3} eV, respectively, indicate that the synchrotron radiation evolves in the fast-cooling regime. Therefore, an optical bright flash with a maximum flux (at the peak) of $F_{\nu,r} \sim F_{\max,r} \left(\frac{\epsilon_\gamma}{\epsilon_{c,r}}\right)^{-\frac{1}{2}} \sim 10^4$ mJy in temporal coincidence with the LAT bright peaks that are similar to that reported for GRB 130427A is expected (see, Kobayashi & Zhang 2003; Fraija et al. 2016b). The maximum flux and the spectral break of the cutoff energy are calculated with the best-fit parameters reported in Table 4 for $\epsilon_\gamma = 1$ eV. Given that the self-absorption energy break is smaller than the cutoff and characteristic ones, the synchrotron emission is in the weak self-absorption regime, and hence a thermal component from the reverse shock cannot be expected (Kobayashi & Zhang 2003). Taking into consideration the fact that the outflow composition is Poynting dominated and the synchrotron emission from the reverse shock is stronger than the radiation originated from the forward shock, polarization is expected in different wavelength bands.

Using the best-fit values we calculate the theoretical fluxes at the maximum fluxes reported by the LAT and GBM instruments. We find that the synchrotron emission from the forward-shock region is ~3 times smaller than the SSC one from the reverse-shock. Once the LAT flux decreases, the synchrotron emission from forward shock begins dominating. Therefore, the SSC emission from the reverse shock can only explain the short-lasting LAT peak and the high-energy photons associated temporally with it, and not the high-energy photons detected at different time intervals ($\gtrsim 10$ s).

The spectral and temporal analysis of the forward and reverse shocks at the beginning of the afterglow phase together the best-fit value of the circumburst density lead to an estimate of the initial bulk Lorentz factor, the critical Lorentz factor and the shock crossing time $\Gamma \simeq 600$, $\Gamma_c \simeq 270$ and $t_d \simeq 4$ s, respectively. The value of the initial bulk Lorentz factor lies in the range of values reported for the luminous LAT-detected GBRs (Veres & Mészáros 2012). This value is consistent with the evolution of reverse shock in the thick-shell case and the duration of the short-lasting LAT and GBM peaks.

The best-fit values found after modeling the LAT, GBM, X-ray, optical, and radio observations with reverse and forward shocks indicate that the high-energy photons originated in external shocks as was previously suggested for others GRBs (Kumar & Barniol Duran 2009, 2010; Zou et al. 2009; Ghisellini et al. 2010; He et al. 2011; Nava et al. 2014; Fraija et al. 2016b, 2017b). It is worth highlighting that the values found of t_0 are in the range of the first high-energy photons detected by Fermi-LAT.

Given the best-fit values of the wind-like and homogeneous medium, the deceleration radius and the bulk Lorentz factor at the transition from the stratified to uniform medium is $R_{tr} \simeq 2.3 \times 10^{17}$ cm and $\Gamma_{tr} \simeq 220$, respectively, which agree with the breaks in the X-ray and optical light curves. In comparison with other bursts that exhibited this transition (GRB 050319, 081109A, and 160626B; Kamble et al. 2007; Jin et al. 2009; Fraija et al. 2017b), the value obtained for GRB 190114C corresponds to the nearest value to the progenitor.

With the best-fit values, we find that the characteristic and cutoff energy breaks the synchrotron emission in the uniform medium at 6×10^3 (6×10^4) s as indicated with dotted lines in the upper panel are 93.2 (5.1) GHz and 166.5 (27.6) keV, respectively. It indicates that during this time interval, X-ray, optical, and radio fluxes evolve in the second PL segment, as shown in Figure 3. The dotted lines mark the period for which the energy breaks were calculated. At 0.2 days, the characteristic and cutoff energy breaks are 22.1 GHZ and 77.6 keV, respectively. This result is consistent with the radio observations reported by Laskar et al. (2019): (i) the optical and radio (ALMA) observations evolved in the similar PL segment and, (ii) the break energy of 24 ± 4 GHz found in the radio spectrum between VLA and ALMA data. In this case this energy break is explained with the characteristic energy calculated in our model.

The Fermi-LAT photon flux light curve of GRB 190114C presented similar features to other bright LAT-detected bursts, as shown in Figure 5. For instance, the equivalent isotropic energy of these bursts was measured to be larger than $>10^{53}$ erg;[10] they exhibited long-lasting emission that was much longer than the prompt phase, and had a short-lasting bright peak located at the beginning of the long-lasting emission (Kumar & Barniol Duran 2009, 2010; Piran & Nakar 2010; Ackermann et al. 2013; Fraija 2015a; Fraija et al. 2016a, 2016b, 2017a, 2017b). All of them presented high-energy photons ($\geqslant 100$ MeV), which arrived delayed alongside the onset of the prompt phase. In addition to exhibiting the previous features, GRB 160625B showed the wind-to-uniform transition. These bursts have been interpreted in the framework of external shocks. The best-fit parameters found for GRB 190114C lie in the range of the values reported in these bursts $0.01 \leqslant \epsilon_{e,f} \leqslant 0.1$, $10^{-5} \leqslant \epsilon_{B,f} \leqslant 10^{-3}$, and $2.15 \leqslant p \leqslant 2.4$. Figure 5 shows that GRB 190114C (red filled stars) is one of the brightest during the first ~100 s and, given that it is the second-closest one, VHE photons are expected from this burst.

5. Conclusions

We have obtained the Fermi-LAT light curve around the reported position of GRB 190114C and showed that it exhibits similar features to the LAT-detected bursts. The first photon detected by the LAT instrument had an energy of 571.4 MeV, arriving at ~2.7 s late with respect to first low-energy photon reported by GBM. The time arrival of this energetic photon is consistent with the starting times of the LAT ($t_0 = 2.61 \pm 0.51$ s) and GBM ($t_0 = 3.09 \pm 0.23$ s) emissions. The highest-energy photons of 10, 21, 6, 19, and 11 GeV detected by the LAT instrument at 18, 21, 32, 36, and 65 s, respectively, after the GBM trigger can be hardly interpreted in the standard synchrotron forward-shock model and some additional mechanisms must be present to interpret the VHE

---

[10] GRB 080916C (Abdo et al. 2009b), GRB 090510 (Ackermann et al. 2010), GRB 090902B (Abdo et al. 2009a), GRB 090926A (Ackermann et al. 2011) GRB 110721A (Ackermann et al. 2013; Fraija et al. 2017a), GRB 110731A (Ackermann et al. 2013), GRB 130427A (Ackermann et al. 2014), and GRB 160625B (Fraija et al. 2017b).
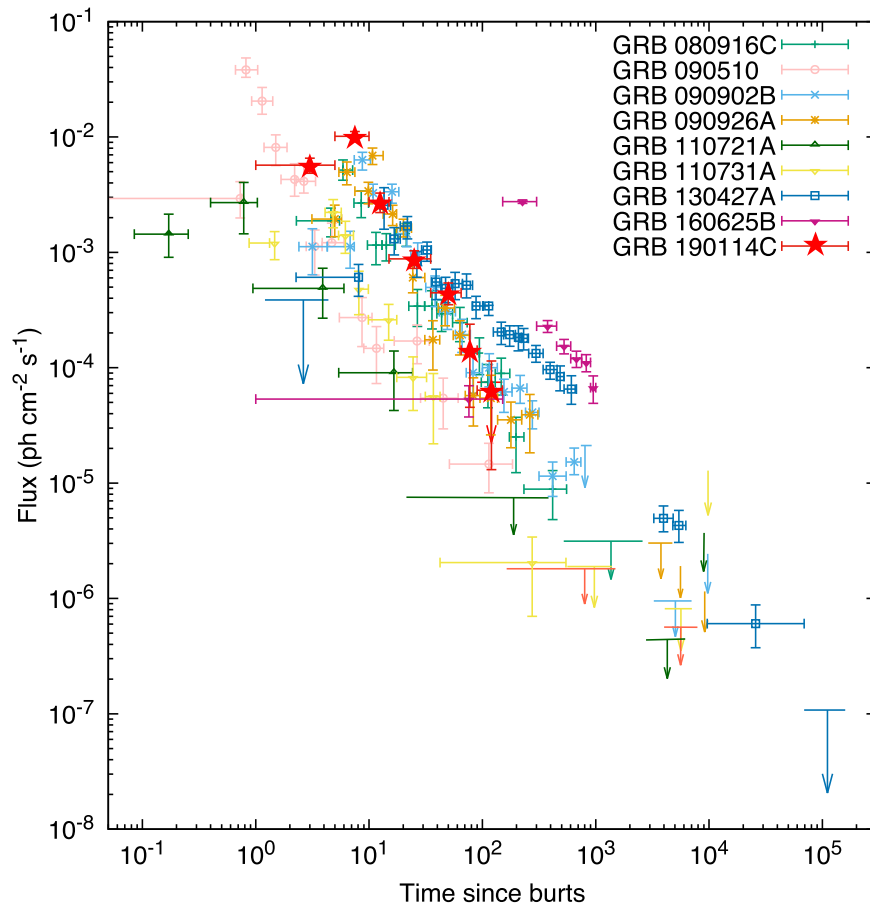
Figure 5. Comparison of the *Fermi*-LAT photon flux light curve from GRB 190114C (red filled stars) with those LAT-detected burst with short-lasting bright peaks and long-lasting emissions. The LAT-detected burst data are taken from Ackermann et al. (2013, 2013, 2014) and Fraija et al. (2017a).

LAT photons. We want to emphasize that the MAGIC-detected photons cannot either be interpreted in the standard synchrotron forward-shock model. The other LAT photons can be explained well by synchrotron emission from the forward shock. The LAT and GBM light curves exhibited a short-lasting bright peak and a long-lasting extended emission. The temporal and spectral indices of the long-lasting extended component are consistent with synchrotron forward-shock model and the short-lasting bright peaks with SSC reverse-shock model. Given the best-fit values, a bright optical flash produced by synchrotron reverse-shock is expected.

The X-ray and optical light curves are consistent with a BPL function with a break at ∼400 s. Using the closure relations and the synchrotron forward-shock model among the LAT, GBM, X-ray, optical, and radio observations, we claim that this break corresponded to a transition phase between a stratified stellar-wind–like and uniform ISM-like medium.

With the values of best-fit values of the stratified and uniform medium, we infer that high-energy observed photons are produced in the deceleration phase of the outflow and a different mechanism of the standard synchrotron model such as SSC emission, photo-hadronic interactions, and proton synchrotron radiation from forward shocks has to be invoked to interpret these VHE photons. Given the values of the microphysical parameters, we claim that the outflow is endowed with magnetic fields.

The best-fit values of the microphysical parameters and the derived value of σ-parameter indicates that an outflow with arbitrary magnetization could explain the features exhibited in the light curves of GRB 190114C (the short-lasting peaks, the "plateau" phase, etc.). Taking into consideration the fact that the ejecta must be magnetized and the synchrotron emission from the reverse shock is stronger than the radiation originated in the forward shock, then polarization in distinct wavelengths is expected.

ORCID iDs

N. Fraija ⓘ https://orcid.org/0000-0002-0173-6453
R. L. Becerra ⓘ https://orcid.org/0000-0002-0216-3415

References

Abdo, A. A., Ackermann, M., Ajello, M., et al. 2009a, ApJL, 706, L138
Abdo, A. A., Ackermann, M., Arimoto, M., et al. 2009b, Sci, 323, 1688
Ackermann, M., Ajello, M., Asano, K., et al. 2011, ApJ, 729, 114

Ackermann, M., Ajello, M., Asano, K., et al. 2013, ApJS, 209, 11
Ackermann, M., Ajello, M., Asano, K., et al. 2014, Sci, 343, 42
Ackermann, M., Asano, K., Atwood, W. B., et al. 2010, ApJ, 716, 1178
Ackermann, M., Ajello, M., Asano, K., et al. 2013, ApJ, 763, 71
Alexander, K. D., Laskar, T., Berger, E., et al. 2019, GCN, 23726, 1
Arnaud, K. A. 1996, in ASP Conf. Ser. 101, Astronomical Data Analysis Software and Systems V, ed. G. H. Jacoby & J. Barnes (San Francisco, CA: ASP), 17
Barniol Duran, R., & Kumar, P. 2011, MNRAS, 412, 522
Becerra, R. L., Dichiara, S., Watson, A. M., et al. 2019a, arXiv:1904.05987
Becerra, R. L., Watson, A. M., Fraija, N., et al. 2019b, arXiv:1901.06051
Becerra, R. L., Watson, A. M., Lee, W. H., et al. 2017, ApJ, 837, 116
Beniamini, P., Nava, L., Duran, R. B., & Piran, T. 2015, MNRAS, 454, 1073
Bolmer, J., & Shady, P. 2019, GCN, 23702, 1
Burenin, R., Bikmaev, I., Irtuganov, E., et al. 2019, GCN, 23766, 1
Castor, J., McCray, R., & Weaver, R. 1975, ApJL, 200, L107
Chevalier, R. A., & Li, Z.-Y. 2000, ApJ, 536, 195
Chevalier, R. A., Li, Z.-Y., & Fransson, C. 2004, ApJ, 606, 369
Dai, Z. G., & Lu, T. 1998, MNRAS, 298, 87
D'Avanzo, P., Covino, S., Fugazza, D., et al. 2019, GCN, 23729, 1
Drenkhahn, G. 2002, A&A, 387, 714
Fan, Y. Z., Wei, D. M., & Wang, C. F. 2004, A&A, 424, 477
Fraija, N. 2015a, ApJ, 804, 105
Fraija, N. 2015b, MNRAS, 450, 2784
Fraija, N. 2014, MNRAS, 437, 2187
Fraija, N., De Colle, F., Veres, P., et al. 2019a, ApJ, 871, 123
Fraija, N., De Colle, F., Veres, P., et al. 2019c, ApJ, submitted (arXiv:1906.00502)
Fraija, N., Lopez-Camara, D., Pedreira, A. C., et al. 2019d, ApJ, submitted (arXiv:1904.07732)
Fraija, N., Lee, W., & Veres, P. 2016a, ApJ, 818, 190
Fraija, N., Lee, W. H., Araya, M., et al. 2017a, ApJ, 848, 94
Fraija, N., Lee, W. H., Veres, P., et al. 2016b, ApJ, 831, 22
Fraija, N., Pedreira, A. C. C. d. E. S., & Veres, P. 2019b, ApJ, 871, 200
Fraija, N., & Veres, P. 2018, ApJ, 859, 70
Fraija, N., Veres, P., Zhang, B. B., et al. 2017b, ApJ, 848, 15
Frederiks, D., Golenetskii, S., Aptekar, R., et al. 2019, GCN, 23737, 1
Fryer, C. L., Rockefeller, G., & Young, P. A. 2006, ApJ, 647, 1269
Fukugita, M., Ichikawa, T., Gunn, J. E., et al. 1996, AJ, 111, 1748
Garcia-Segura, G., & Franco, J. 1996, ApJ, 469, 171
Ghisellini, G., Ghirlanda, G., Nava, L., & Celotti, A. 2010, MNRAS, 403, 926
Giblin, T. W., van Paradijs, J., Kouveliotou, C., et al. 1999, ApJL, 524, L47
Granot, J. 2003, ApJL, 596, L17
Gropp, J. D., Kennea, J. A., Klinger, N. J., et al. 2019, GCN, 23688, 1
Hamburg, R., Veres, P., Meegan, C., et al. 2019, GCN, 23707, 1
He, H.-N., Wu, X.-F., Toma, K., Wang, X.-Y., & Mészáros, P. 2011, ApJ, 733, 22
Im, M., Paek, G. S., Kim, S., et al. 2019a, GCN, 23717, 1
Im, M., Paek, G. S. H., Choi, C., et al. 2019b, GCN, 23740, 1
Izzo, L., Noschese, A., D'Avino, L., et al. 2019, GCN, 23699, 1
Jin, Z. P., Xu, D., Covino, S., et al. 2009, MNRAS, 400, 1829
Kamble, A., Resmi, L., & Misra, K. 2007, ApJL, 664, L5
Kim, J., & Im, M. 2019a, GCN, 23732, 1
Kim, J., Im, M., Lee, C.-U., et al. 2019b, GCN, 23734, 1
Kobayashi, S. 2000, ApJ, 545, 807

Kobayashi, S., & Zhang, B. 2003, ApJ, 597, 455
Kobayashi, S., & Zhang, B. 2007, ApJ, 655, 973
Kocevski, D., Omodei, N., Axelsson, M., et al. 2019, GCN, 23709, 1
Krimm, H. A., Barthelmy, S. D., Cummings, J. R., et al. 2019, GCN, 23724, 1
Kumar, H., Srivastav, S., Waratkar, G., et al. 2019, GCN, 23733, 1
Kumar, P., & Barniol Duran, R. 2009, MNRAS, 400, L75
Kumar, P., & Barniol Duran, R. 2010, MNRAS, 409, 226
Kumar, P., & Panaitescu, A. 2000, ApJL, 541, L51
Kumar, P., & Piran, T. 2000, ApJ, 532, 286
Kumar, P., & Zhang, B. 2015, PhR, 561, 1
Laskar, T., Alexander, K. D., Gill, R., et al. 2019, ApJL, 878, L26
Lipunov, V., Tyurina, N., Kuznetsov, A., et al. 2019, GCN, 23693, 1
Mazaeva, E., Pozanenko, A., Volnova, A., et al. 2019, GCN, 23741, 1
Melandri, A., Izzo, L., D'Avanzo, P., et al. 2019, GCN, 23983, 1
Minaev, P., & Pozanenko, A. 2019, GCN, 23714, 1
Mirzoyan, R., et al. 2019, GCN, 23701, 1
Nava, L., Vianello, G., Omodei, N., et al. 2014, MNRAS, 443, 3578
Osborne, J. P., Beardmore, A. P., Evans, P. A., et al. 2019, GCN, 23704, 1
Panaitescu, A., & Kumar, P. 2000, ApJ, 543, 66
Panaitescu, A., & Mészáros, P. 1998, ApJL, 493, L31
Pe'er, A., & Wijers, R. A. M. J. 2006, ApJ, 643, 1036
Piran, T., & Nakar, E. 2010, ApJL, 718, L63
Planck Collaboration, Aghanim, N., Akrami, Y., et al. 2018, arXiv:1807.06209
Ravasio, M. E., Oganesyan, G., Salafia, O. S., et al. 2019, A&A, 626, A12
Sari, R., & Piran, T. 1995, ApJL, 455, L143
Sari, R., & Piran, T. 1999, A&AS, 138, 537
Sari, R., Piran, T., & Narayan, R. 1998, ApJL, 497, L17
Selsing, J., Fynbo, J. P. U., Heintz, K. E., et al. 2019, GCN, 23695, 1
Siegel, M. H., & Gropp, J. D. 2019, GCN, 23725, 1
Stratta, G., Dainotti, M. G., Dall'Osso, S., Hernandez, X., & Cesare, G. De 2018, ApJ, 869, 155
Troja, E., Lipunov, V. M., Mundell, C. G., et al. 2017, Natur, 547, 425
Tyurina, N., Lipunov, V., Kuznetsov, A., et al. 2019, GCN, 23690, 1
de Ugarte Postigo, A., Kann, D. A., Thoene, C. C., & Izzo, L. 2019, GCN, 23692, 1
Uhm, Z. L., & Zhang, B. 2014, NatPh, 10, 351
Ursi, A., Tavani, M., Marisaldi, M., et al. 2019, GCN, 23712, 1
Vaughan, S., Goad, M. R., Beardmore, A. P., et al. 2006, ApJ, 638, 920
Veres, P., & Mészáros, P. 2012, ApJ, 755, 12
Vestrand, W. T., Wren, J. A., Wozniak, P. R., et al. 2006, Natur, 442, 172
Vink, J. S., & de Koter, A. 2005, A&A, 442, 587
Vink, J. S., de Koter, A., & Lamers, H. J. G. L. M. 2000, A&A, 362, 295
Wang, X. Y., Dai, Z. G., & Lu, T. 2001a, ApJL, 546, L33
Wang, X. Y., Dai, Z. G., & Lu, T. 2001b, ApJ, 556, 1010
Wang, Y., Li, L., Moradi, R., & Ruffini, R. 2019, arXiv:1901.07505
Weaver, R., McCray, R., Castor, J., Shapiro, P., & Moore, R. 1977, ApJ, 218, 377
Xiao, S., Li, C. K., Li, X. B., et al. 2019, GCN, 23716, 1
Zhang, B., Fan, Y. Z., Dyks, J., et al. 2006, ApJ, 642, 354
Zhang, B., & Kobayashi, S. 2005, ApJ, 628, 315
Zhang, B., Kobayashi, S., & Mészáros, P. 2003, ApJ, 595, 950
Zhang, B., & Mészáros, P. 2004, IJMPA, 19, 2385
Zhang, B., & Yan, H. 2011, ApJ, 726, 90
Zou, Y.-C., Fan, Y.-Z., & Piran, T. 2009, MNRAS, 396, 1163